Chemical Engineering Journal 474 (2023) 145675

Contents lists available at ScienceDirect

Chemical Engineering Journal

journal homepage: www.elsevier.com/locate/cej

Theoretical calculation-guided engineering of Fe-Mn based dual-center single-atom catalysts for synergistic tumor therapy

Xueyang Fang [a,b,1], Decai Yang [a,*,1], Xianlin Wu [c,d,1], Kwok-Ho Lui [b], Xin Li [b], Wai-Sum Lo [b], Chenxi Li [a], Yuanyuan Zhang [a], Guohui Nie [a], Lijun Jiang [e,*], Yanjuan Gu [b,*], Bin Zhang [a,*], Wing-Tak Wong [b,*]

[a] Shenzhen Institute of Translational Medicine, Shenzhen Second People's Hospital, The First Affiliated Hospital of Shenzhen University, Guangdong Key Laboratory for Biomedical Measurements and Ultrasound Imaging, National-Regional Key Technology Engineering Laboratory for Medical Ultrasound, School of Biomedical Engineering, Shenzhen University Medical School, Shenzhen 518035, China
[b] Department of Applied Biology and Chemical Technology, The Hong Kong Polytechnic University, Hong Kong Special Administrative Region
[c] Cancer Center, Shenzhen Hospital of Guangzhou University of Chinese Medicine, Shenzhen 518000, China
[d] Institute of Clinical Medicine, The First Affiliated Hospital of Jinan University, Guangzhou 510632, China
[e] Hubei Key Laboratory of Genetic Regulation & Integrative Biology, School of Life Sciences, Central China Normal University, Wuhan 430079, China

ARTICLE INFO

Keywords:
Dual single-atom catalysts
Tumor microenvironment
H_2O_2 activation
Hypoxia alleviation
Synergistic cancer therapy

ABSTRACT

Tumor therapy employing metal-based nanomaterials to convert the abundant H_2O_2 in tumor microenvironment (TME) to oxygen (O_2) and hydroxy radical (·OH) has attracted substantial attention. However, the generally complex structure of metal nanosystems may have poor catalytic selectivity towards the target and hence cause undesired side reactions. Single-atom catalysts (SACs) with high atomic utilization, composition of identical active site and tunable reaction pathway can be harnessed to realize the well-controlled and highly-selective conversion of H_2O_2 for cancer therapy. Herein, a series of dual single-atom catalysts (DSACs) containing two metal centers (Fe-Se_6, Mn-Se_6) are proposed. As guided by theoretical calculations, DSACs with equal proportions of Fe and Mn (termed as Fe/Mn@PSe_3) exhibit the optimal reaction barriers towards the production of both ·OH and O_2 by catalyzing H_2O_2. In response to the elevated TME H_2O_2, Fe/Mn@PSe_3 can produce ·OH to trigger chemodynamic therapy (CDT), and boost O_2 generation to alleviate tumor hypoxia and its mediated immunosuppression. In addition, its mild hyperthermia feature enhances the anti-tumor effects of CDT and immune therapy, causing an efficient synergistic tumor suppression outcome. The study provides new insights into highly selective nanomaterial design that preferentially activating specific catalytic processes within tumor, functioning as promising candidates for cancer therapy.

1. Introduction

Tumor microenvironment (TME) plays a crucial role in controlling cancer development, progression, metastasis, as well as resistance towards cancer therapy [1]. The key features of TME could be utilized to develop highly effective and selective strategies to combat cancer, which theoretically won't cause any significant damage to normal cells [2]. Hypoxia is a common feature in TME, and is well-known to negatively impair the efficacy of oxygen-dependent cancer therapies, including the clinically used photodynamic therapy and radiotherapy [3,4]. Tumor cells can adapt to hypoxia stress, and this is mainly facilitated by a transcriptional regulation family, the hypoxia-inducible factors (HIFs). It has been well-established that HIFs mediate angiogenesis, metabolism, and apoptosis, contributing to tumor progression, metastasis, and therapy resistance. Beyond HIFs, hypoxia also attracts immunosuppressive cells such as T regulatory cells (Tregs), exerting a negative impact on immunotherapy [5–7]. As another salient feature of TME, the high level of hydrogen peroxide (H_2O_2), originating from the uncontrolled metabolism during hyperliferation, has also been exploited for cancer therapy [8], which is highly beneficial to alleviate TME hypoxia

* Corresponding authors.
E-mail addresses: yangdecai_cn@163.com (D. Yang), lijunjiang@ccnu.edu.cn (L. Jiang), yanjuan.gu@polyu.edu.hk (Y. Gu), binzhang@email.szu.edu.cn (B. Zhang), w.t.wong@polyu.edu.hk (W.-T. Wong).
[1] X. Fang, D. Yang and X. Wu contributed equally.

https://doi.org/10.1016/j.cej.2023.145675
Received 27 April 2023; Received in revised form 28 July 2023; Accepted 25 August 2023
Available online 30 August 2023

by catalyzing endogenous H_2O_2 to produce O_2 [9]. Among them, the recently emerged catalytic therapy which employs nanocatalysts for converting endogenous H_2O_2 to O_2 or reactive oxygen species (ROS) has attracted extensive attention from researchers. In this endeavor, one approach is the conversion of H_2O_2 to O_2 to counter tumor hypoxia and therefore reverse hypoxia-induced immunosuppression, the other is to convert H_2O_2 to the highly cytotoxic hydroxyl radical (·OH) *via* Fenton-like pathways to enable chemodynamic therapy (CDT). Although examples of nanomaterials converting H_2O_2 into ·OH and O_2 in TME simultaneously for specific and efficient cancer therapy have been reported [10,11], strategies for the design and construction of a nanoplatform with tunable catalytic activity towards the production of ·OH or O_2 from H_2O_2 have not been explored in-depth.

As there are different pathways of H_2O_2 decomposition, it is of great significance to gain a clear understanding of the relationship between composition, structure, and properties of the catalyst, which is also important for the improvement of therapeutic effect and biosafety profile. Transition metal-based catalysts are well-known for their capabilities in facilitating H_2O_2 activation [12]. Representative examples are seen in the low-toxic essential trace elements Fe and Mn. Compared with metal nanoparticles where the atomic sites may vary in activity due to different coordination environments, metal sites in single-atom catalysts (SACs) are exclusively dispersed as isolated single atoms *via* coordinating with surrounding atoms from the support, and SACs have become a new frontier of heterogeneous catalysis [13,14]. The dispersal of single transition metal atoms on host materials in SACs presents an unsaturated coordination environment and allows identical catalytic centers, featuring high catalytic activity and controlled selectivity. SACs with intrinsic enzyme-like properties are a novel type of nanozymes and have been exploited for tumor theranostics [15,16]. For example, a nanocatalyst with the single-atom Fe_1-N_4 active center, regarded as peroxidase (POD)-like nanozyme, can efficiently catalyze endogenous H_2O_2 to ·OH through Fenton-like reactions, leading to an impressive tumor suppression outcome [17]. Mn-based SACs have also attracted much attention due to their coordination-dependent multi-enzyme activities. For example, single Mn atoms coordinated to three N atoms could perform as catalase-like nanozymes to catalyze the production of ·OH and O_2 from H_2O_2 in acidic conditions [18]. Besides, uniform catalytic centers with high selectivity offer an ideal platform for examining the reaction mechanisms. Despite these advantages, it may be difficult for SACs to realize multiple catalytic functions because of their monotonous metal sites. Therefore, incorporating additional active sites with a second atomically dispersed metal species is an attractive approach to further improve the catalytic action of SACs and endow the well-defined materials with more catalytic potential due to the electronic interaction between the support and the two different metals. The so-called dual single-atom catalysts (DSACs), benefiting from the synergistic effect between dual active sites, could deliver a superior catalytic performance, and have been widely employed in areas from chemical engineering industry to biomedical applications [19–22]. For example, a Fe-Mn based SACs, was recently developed for parallel catalytic "ROS cycle" for cancer therapy [22]. However, the catalytic performance and therapeutic potential of a DSAC constructed from the two typical transition metals in the field, Fe and Mn, for activating H_2O_2 have not been well studied yet.

Herein, we describe the rational design and construction of Fe-Mn-based DSACs for dual catalytic activities and tunable selectivity for the effective synergistic cancer therapy. Guided by theoretical calculations, DSACs with equal proportions of Fe and Mn, termed as Fe/Mn@PSe_3, present the lowest reaction barriers towards the production of both ·OH and O_2 by catalyzing H_2O_2. In response to the elevated H_2O_2 level in TME, Fe/Mn@PSe_3 nanocomposites are expected to catalyze the production of ·OH to trigger CDT, and to boost O_2 generation to alleviate tumor hypoxia and its mediated immunosuppression. Tumor-suppressing effects can be further improved by mild photothermal-augmented chemodynamic/immune therapy. Taken together, we present a practical paradigm for synergistic cancer treatment with reduced side effects due to the well-controlled catalytic actions (activity & selectivity) and the nontoxic nature of the designed DSACs (Scheme 1).

2. Results and discussion

2.1. DFT studies on the catalytic performance of Fe/Mn@PSe_3

Fe@PSe_3 and Mn@PSe_3 have been reported to demonstrate good anti-tumor behaviors [23,24], but the correlation between the catalytic mechanisms and the biomedical applications lacks theoretical clarification. In this regard, DFT calculations were conducted on the decomposition process of H_2O_2. The six-coordinated metal centers over PSe_3 nanosheets were adopted as the model, and the calculated pathways over Fe/Mn@PSe_3 with different Fe/Mn molar ratios are depicted in Fig. 1. The proposed catalytic pathways are shown in Fig. 1C, including the substrate and intermediates absorbed on a given catalyst. Compared with Fe and Mn SACs (Fig. 1A and 1F) where the chemical valences for both metal elements are + 2, pathway 2 leading to ·OH formation is predominant, while pathway 1 converts H_2O_2 into O_2 exhibited an energy barrier for both SACs (0.24 eV for Fe@PSe_3 and 2.38 eV for Mn@PSe_3) in the rate-limiting step (OOH + H → O_2 + 2H), suggesting that Se-coordinated metal atoms behaved differently compared to N-coordinated ones as indicated in literature [18]. This means, from the perspective of thermodynamics, the catalytic Fenton-like reactions in both SACs occur spontaneously at ambient conditions, but an additional driving force (pH, temperature, etc.) is required for the O_2 generation.

To check whether the introduction of other metal atoms can alter the catalytic pathway like metal alloys, additional calculations were performed over three DSACs with Fe/Mn molar ratios of 3/1 ($Fe_{0.75}Mn_{0.25}$@PSe_3, Fig. 1B), 1/1 ($Fe_{0.5}Mn_{0.5}$@PSe_3, Fig. 1D) and 1/3 ($Fe_{0.25}Mn_{0.75}$@PSe_3, Fig. 1E). When performing the calculations, the reactants, intermediates and products were placed at a bridge position between Fe and Mn to check the competitive absorption ability of both metals, the result of which showed that different ratios would lead to different absorption behavior, yielding different catalytic pathways. As expected, the $Fe_{0.25}Mn_{0.75}$@PSe_3 showed similar absorption energy profile to that of Mn/PSe_3 as Mn dominates in this material. Interestingly, when Fe takes up most of the active sites, a drastically different result was observed. The result of $Fe_{0.75}Mn_{0.25}$@PSe_3 manifests that when 25% of Fe sites were replaced with Mn, the catalytic conversion following pathway 2 becomes much more energetically favorable. After checking the calculated energic profiles of $Fe_{0.5}Mn_{0.5}$@PSe_3 (Fig. 1D), it is found that both pathways showed a reaction barrier of 0.29 eV prior to the rate-limiting step (OOH + H → O_2 + 2H) for pathway 1 and that oxygen generation becomes exothermic and occurs spontaneously. Such a phenomenon might be due to the interaction among Fe-Se-Mn drastically that alters the electron cloud density at this ratio, thus endowing new absorption energy files and resulting in a special pathway. This means that as long as the 0.29 eV barrier is overcome *via* heating or decreasing the application pH values, H_2O_2 can be transformed into both O_2 and ·OH readily without further stimulation. These calculations successfully demonstrated that the structure composition greatly influences the catalytic selectivity and activity for H_2O_2, and the easily transformed energy profiles during the reaction process highlighted the significance of well-configured SACs in mechanistic studies. Based on the above structure-performance analysis, $Fe_{0.5}Mn_{0.5}$@PSe_3 (named as Fe/Mn@PSe_3 hereafter) was employed for evaluating the catalytic results and synergistic anti-tumor behaviors.

2.2. Fabrication of the dual-metal single-atom catalyst Fe/Mn@PSe_3

The fabrication of Fe/Mn@PSe_3 is displayed in Fig. 2A. In brief, the multi-layer Fe/Mn@PSe_3 was prepared through a chemical vapor transport process, followed by the sonicate exfoliation to obtain the

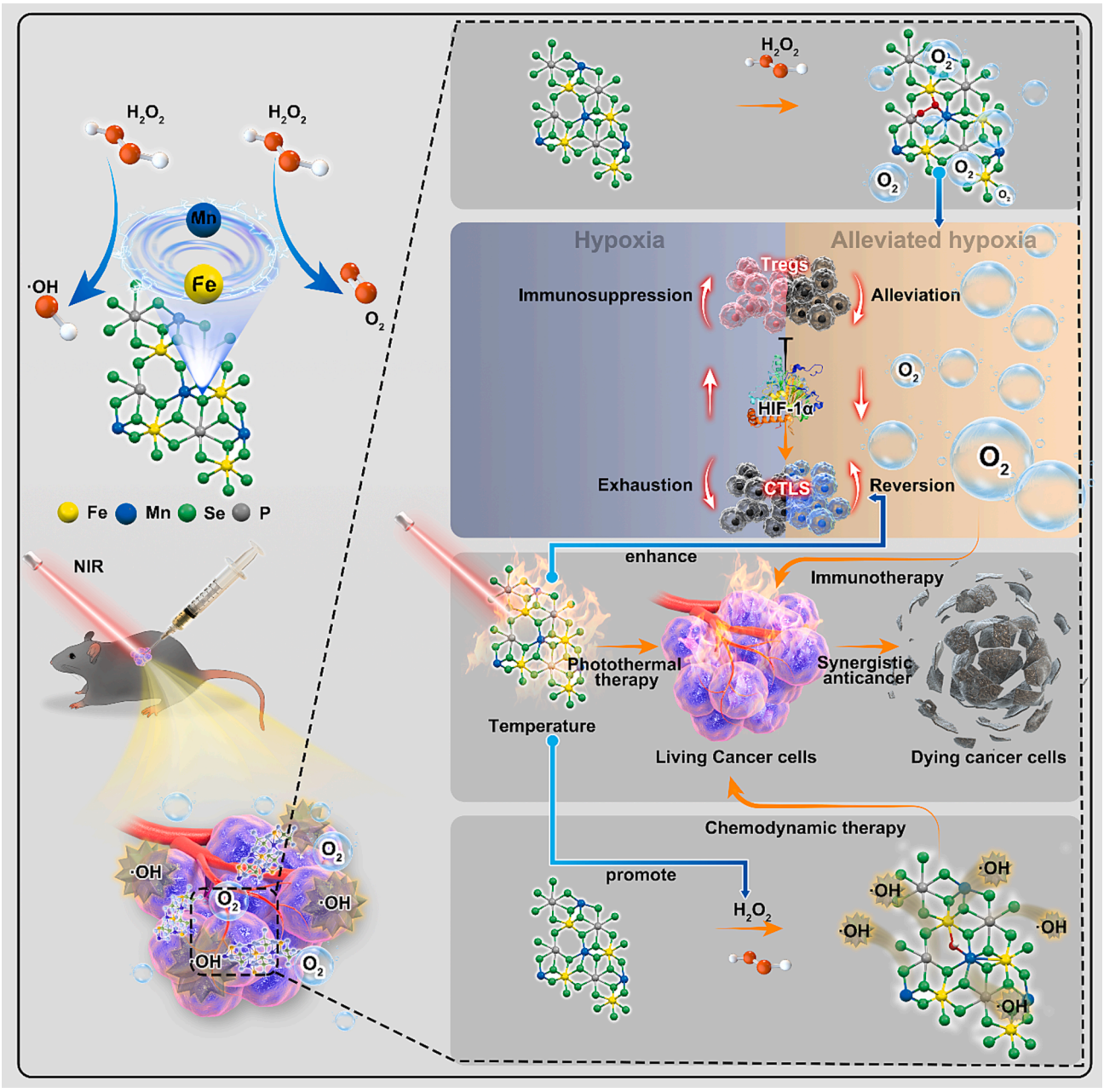

Scheme 1. A schematic diagram showing the working mechanisms of Fe/Mn@PSe_3 nanocomposites for synergistic cancer therapy.

nanosheet structure of Fe/Mn@PSe_3. Morphology of the bulk samples of Fe/Mn@PSe_3 was measured using scanning electron microscopy (SEM), where the multilayer structure can be clearly observed with a size larger than 20 μm (Fig. 2B). According to energy dispersive analysis (Fig. S1), the bulk crystals consisted of elements Fe, Mn, P, and Se. Exfoliation of Fe/Mn@PSe_3 nanocomposites was processed according to experimental section. Size and dispersion of the nanocomposites were measured by scanning transmission electron microscopy (STEM) and dynamic light scattering (DLS), and found to be around 105 nm with a good size distribution (Fig. 2C-D). Note that the excellent stability of Fe/Mn@PSe_3 nanocomposites in physiological conditions, e.g. PBS, DMEM, and DMEM + FBS, have also been measured and confirmed by DLS (Fig. S2). Ultrathin thickness of the nanocomposites was confirmed and determined to be 7 ~ 8 nm by atomic force microscopy (AFM), as displayed in Fig. 2E. A representative image of the exfoliated Fe/Mn@PSe_3 nanocomposites captured under scanning transmission electron microscopy-dark field (STEM-DF) and corresponding elemental mapping are shown in Fig. 2F and S3, which revealed the elemental composition: Fe, Mn, P, and Se. The lattice fringe spacings of 0.301 and 0.634 nm marked in Fig. 2G were indexed to (121) and (001) facets of Fe/Mn@PSe_3 nanocomposites, respectively, suggesting the retainment of the initial composition of the bulk Fe/Mn@PSe_3 after exfoliation, which is consistent with the X-Ray Diffraction (XRD) results (Fig. S4). The aberration-corrected high-angle annular dark-field scanning transmission electron microscopy (AC HAADF-STEM) image with atomic resolution confirmed that the isolated Fe and Mn atoms were anchored on the PSe_3 support (Fig. 2H). Besides elemental mapping, peaks corresponding to elements Fe, Mn, P and Se can also be clearly seen in the XPS spectra of Fe/Mn@PSe_3 nanocomposites (Fig. 2I). Mixed valence states were observed for both Fe and Mn in Fe/Mn@PSe_3, and their lower oxidation state (+2) was dominant (Fig. 2J-K), which indicates the charge transfer between metal species and the support.

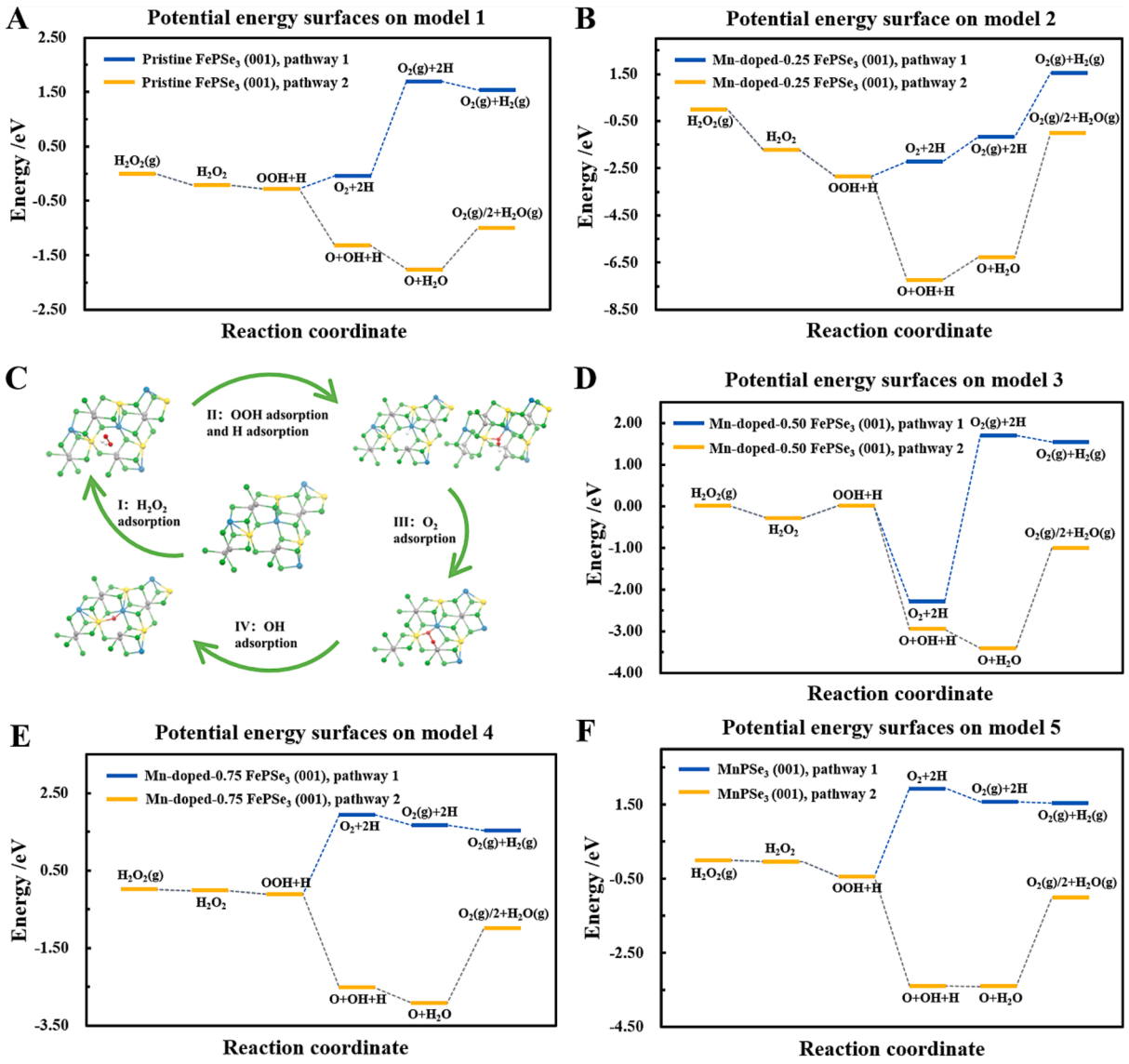

Fig. 1. DFT studies on the decomposition process of H_2O_2 by Fe-Mn single-atom catalyst with varying Fe/Mn molar ratios: (A) Fe SACs, model 1; (B) $Fe_{0.75}Mn_{0.25}@PSe_3$, model 2; (D) Fe/Mn@PSe_3, model 3; (E) $Fe_{0.25}Mn_{0.75}@PSe_3$, model 4 and (F) Mn SACs, model 5. (C) Schematic illustration of the proposed reaction mechanism of H_2O_2 decomposition to O_2 and ·OH by Fe/Mn@PSe_3.

2.3. Structural characterization revealing the single atomic nature of Fe and Mn in Fe/Mn@PSe_3

To further characterize the oxidation states of Fe and Mn in Fe/Mn@PSe_3 and their catalytic ability, X-ray absorption near-edge structure (XANES) spectra of our Fe/Mn@PSe_3 and Fe standard compounds possessing different oxidation states were measured and analyzed (Fig. 3B). By comparing the absorption features and intensities of Fe/Mn@PSe_3 with the reference samples, we infer the major oxidation state of Fe ions in Fe/Mn@PSe_3 is + 2, which is well consistent with observations in the XPS spectra. Similarly, oxidation state of Mn ions is suggested to be + 2 (Fig. 3C). Moreover, the extended X-ray absorption fine structure (EXAFS) was employed to provide detailed information of the local coordination environment of Fe and Mn in Fe/Mn@PSe_3. Characteristic peaks corresponding to Fe-Se and Mn-Se bonds appeared in the Fourier-transformed EXAFS profiles of Fe/Mn@PSe_3 nanocomposites in R space, while no detectable Fe-Fe or Mn-Mn characteristic peaks demonstrated compared with the Fe foil and Mn foil (Fig. 3D-E and S5). Besides, Fe-Se and Mn-Se bond lengths inside Fe/Mn@PSe_3 are 2.64 Å and 2.71 Å, respectively, consistent with previous Fe-Se and Mn-Se studies [25,26], which differ from Fe-Fe inside Fe foil and Mn-Mn inside Mn foil (Table S1). In addition, the maxima of wavelet transform (WT) for Fe/Mn@PSe_3 were assigned to Fe-Se and Mn-Se coordination, respectively (Fig. 3F-G), which is different for Fe foil and Mn foil shown in Fig. S6. These results clearly demonstrated the absence of Fe-Fe, Fe-Mn or Mn-Mn bond from the structure and confirmed the atomically dispersed Fe and Mn in Fe/Mn@PSe_3 nanocomposites, hinting at their high catalytic activity.

2.4. Mild hyperthermia features

We next examined the photothermal performance of Fe/Mn@PSe_3 nanocomposites. Vis-NIR absorbance spectra of Fe/Mn@PSe_3 nanocomposites showed a concentration-dependent broad absorption band (Fig. S7A). To measure its photothermal performance, Fe/Mn@PSe_3 at different concentrations were irradiated by an 808 nm NIR laser under varied densities of power. Changes in temperature were measured using a thermal imager. Upon irradiation, the temperature of Fe/Mn@PSe_3 increased in a concentration- and power density-dependent manner (Fig. S7B-D). In detail, the temperature was raised up to 31.0 °C, 40.7 °C,

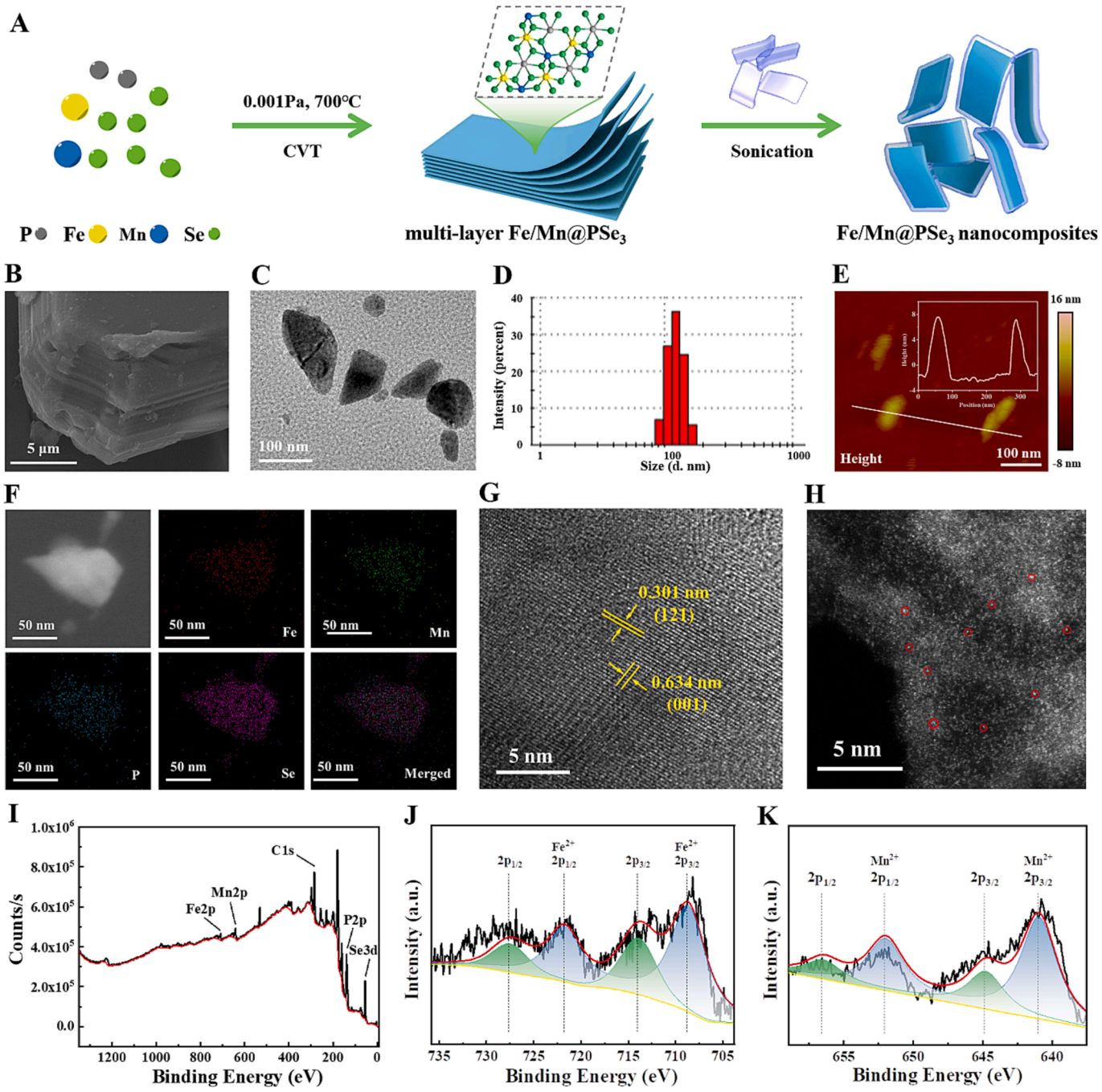

Fig. 2. Fabrication and characterization of Fe/Mn@PSe_3 nanocomposites. (A) Schematic illustration of the preparation of Fe/Mn@PSe_3. (B) Representative SEM image showing the multilayer structure of Fe/Mn@PSe_3 bulk crystal. (C) STEM image, (D) DLS measurement, and (E) AFM image of Fe/Mn@PSe_3; inset in (E), height analysis of ultrathin Fe/Mn@PSe_3. (F) STEM-DF image and corresponding elemental mapping of Fe/Mn@PSe_3. (G) HRTEM image of Fe/Mn@PSe_3. (H) AC HAADF-STEM image of Fe/Mn@PSe_3; the isolated bright dots are single Fe/Mn atoms. (I) XPS spectrum of Fe/Mn@PSe_3. (J, K) High-resolution XPS spectrum of Fe 2p and Mn 2p electrons.

56.6 °C, 64.3 °C for concentrations of 62.5 ppm, 125 ppm, 250 ppm, 500 ppm, respectively. And, exposure to the highest laser power density (2 W/cm^2) caused a more profound temperature increase compared to other groups. In addition, no loss of photothermal conversion efficiency was observed during the three consecutive heating/cooling cycles of Fe/Mn@PSe_3, demonstrating its good photothermal stability (Fig. S7E). The photothermal conversion efficiency (η) was estimated to be 15.6% (Fig. S7F). The atomically dispersed Fe/Mn dual metal sites and the mild hyperthermia features inspired us to evaluate the catalytic ability of Fe/Mn@PSe_3 in activating H_2O_2.

2.5. *Bidirectional H_2O_2 activation*

As demonstrated by the DFT results, the Fe/Mn@PSe_3 nanocomposites with Fe and Mn at a molar ratio of 1:1 can efficiently catalyze H_2O_2 to ·OH and O_2 simultaneously, thus enabling the bidirectional activation of H_2O_2 as illustrated in Fig. 3A. Single-atom catalyst Fe@PSe_3 and Mn@PSe_3 was also prepared to study and compare their catalytic activity in producing ·OH and O_2. 3,3′,5,5′-tetramethylbenzidine (TMB) was used as a probe to detect the production of ROS by colorimetric reaction, as it can be oxidized by ROS to oxTMB with absorption maximum at 652 nm. Absorbance spectrum of different

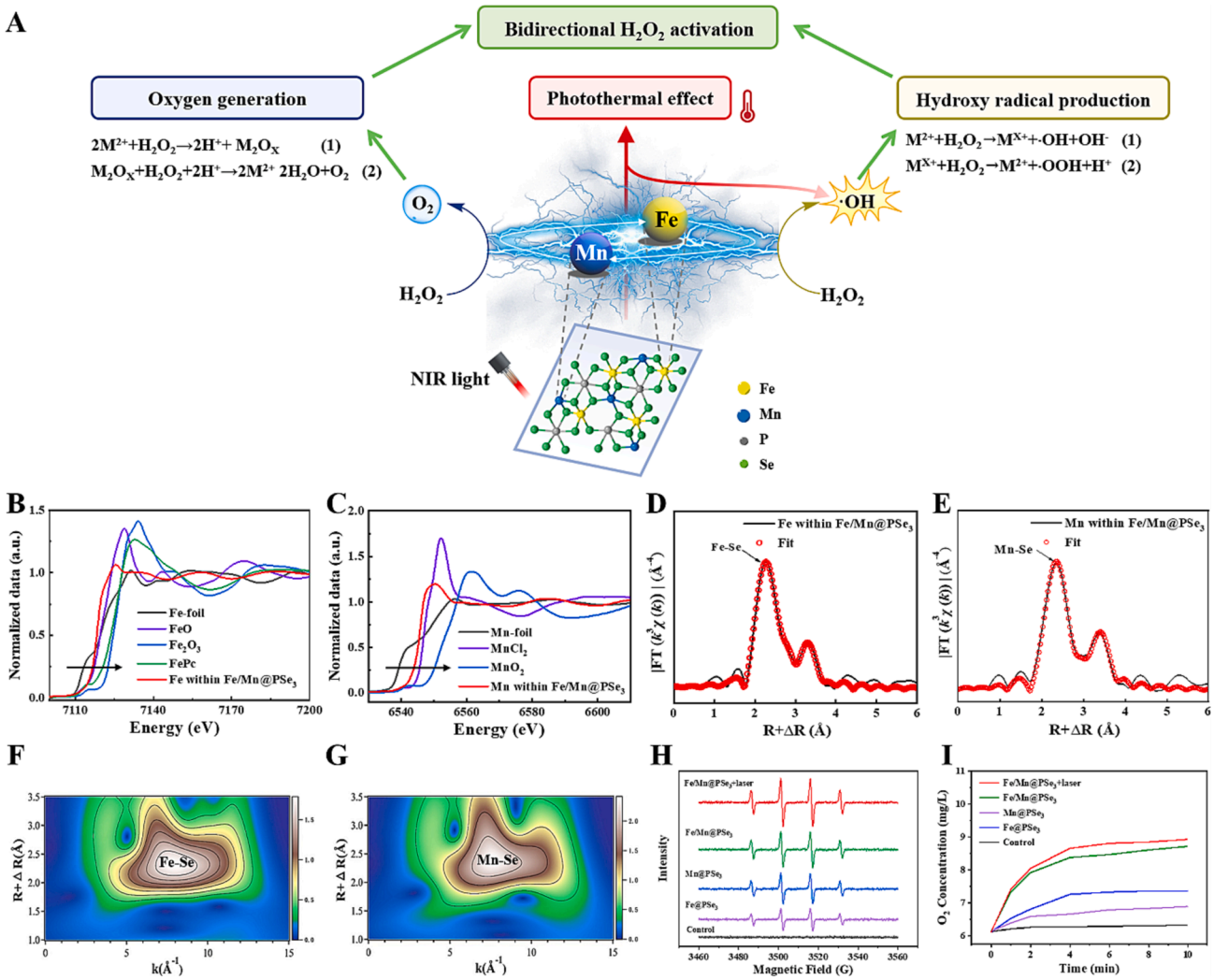

Fig. 3. (A) Schematic illustration of Fe/Mn@PSe_3 nanocomposites for bidirectional H_2O_2 activation. The photothermal-accelerated ·OH production is also included as shown with red arrows. (B-C) XANES spectra at (B) Fe K-edge and (C) Mn K-edge of Fe/Mn@PSe_3 and reference samples. (D, E) EXAFS spectrum and fitting result in R space at (D) Fe and (E) Mn K-edge for Fe/Mn@PSe_3. (F, G) Wavelet transform of (F) Fe and (G) Mn K-edge EXAFS for Fe/Mn@PSe_3. (H) ·OH production detected by electron spin resonance (ESR) spectra. (I) O_2 produced from different treatment groups.

treatment groups in simulated TME was measured using a UV–vis spectrophotometer (Fig. S8). As can be seen, a greater ROS generation is seen with Fe/Mn@PSe_3 than Mn@PSe_3 or Fe@PSe_3, verifying equal portions of Fe and Mn can efficiently catalyze H_2O_2 to produce ROS and can be further enhanced under laser irradiation. To make the enzymatic reaction mechanism of Fe/Mn@PSe_3 clear, we further checked the generation of active intermediate by ESR spectroscopy, where 5,5-dimethyl-1-pyrroline N-oxide (DMPO) was employed as the trapping agent. As shown in Fig. 3H, ·OH is the main product during the catalytic process, and when compared with different treatment groups, a similar trend was shown, confirming that Fe/Mn@PSe_3 exhibits the optimal reaction barriers to catalyze H_2O_2 to generate ·OH. Enzymatic kinetic experiments were also conducted according to procedures described in the literature [27–29]. Fe/Mn@PSe_3 exhibited good POD-like catalytic activity at pH 6.5, Michaelis-Menton constant (K_m) and maximum reaction rate (V_{max}) of Fe/Mn@PSe_3 at pH 6.5 were measured to be 0.17 mM and 2.73×10^{-8} M s^{-1}, respectively (Fig. S9).

Catalytic production of O_2 by Fe/Mn@PSe_3 was also measured with the comparison to the two single-atom catalysts. As shown in Fig. 3I, a greater amount of O_2 is produced upon treatment with Fe/Mn@PSe_3 than Mn@PSe_3 or Fe@PSe_3, which suggests Fe/Mn@PSe_3 has better catalytic activity towards O_2 production, indicating it has a potential role in alleviating tumor hypoxia.

2.6. Intracellular ROS generation and cytotoxicity

Encouraged by the mild hyperthermia and bidirectional H_2O_2 activation features, the *in vitro* anti-cancer effect of Fe/Mn@PSe_3 nanocomposites was determined by MTT assay. A more significant cytotoxicity is observed for Fe/Mn@PSe_3 treatment on CT26 cancer cells in simulated TME compared to in normal condition (Fig. 4A and Fig. S10). The enhanced cytotoxicity can be attributed to the greater ROS generation by Fe/Mn@PSe_3 in the simulated TME, which therefore leading to an improved CDT effect. Similar to situations in the normal condition, cytotoxicity can be further enhanced when irradiated with NIR laser, demonstrating that the CDT effect can be augmented by mild-hyperthermia performance of the nanocomposites. Two normal cell lines, human umbilical vein endothelial cell (HUVECs) and embryonic fibroblast cells (NIH 3 T3), were also used to evaluate the biosafety of Fe/Mn@PSe_3 nanocomposites. As shown in Fig. S11, no obvious cytotoxicity can be found for Fe/Mn@PSe_3. The *in vitro* anti-cancer effect can also be directly visualized by confocal laser scanning microscopy imaging of the treated cells which were co-stained with fluorescent probes calcein AM (for live cells, in green fluorescence) and PI (for dead cells staining, in red fluorescence). Treatment with Fe/Mn@PSe_3 + laser exhibited the strongest red fluorescence compared to Fe/Mn@PSe_3 or laser alone treated groups (Fig. 4B).

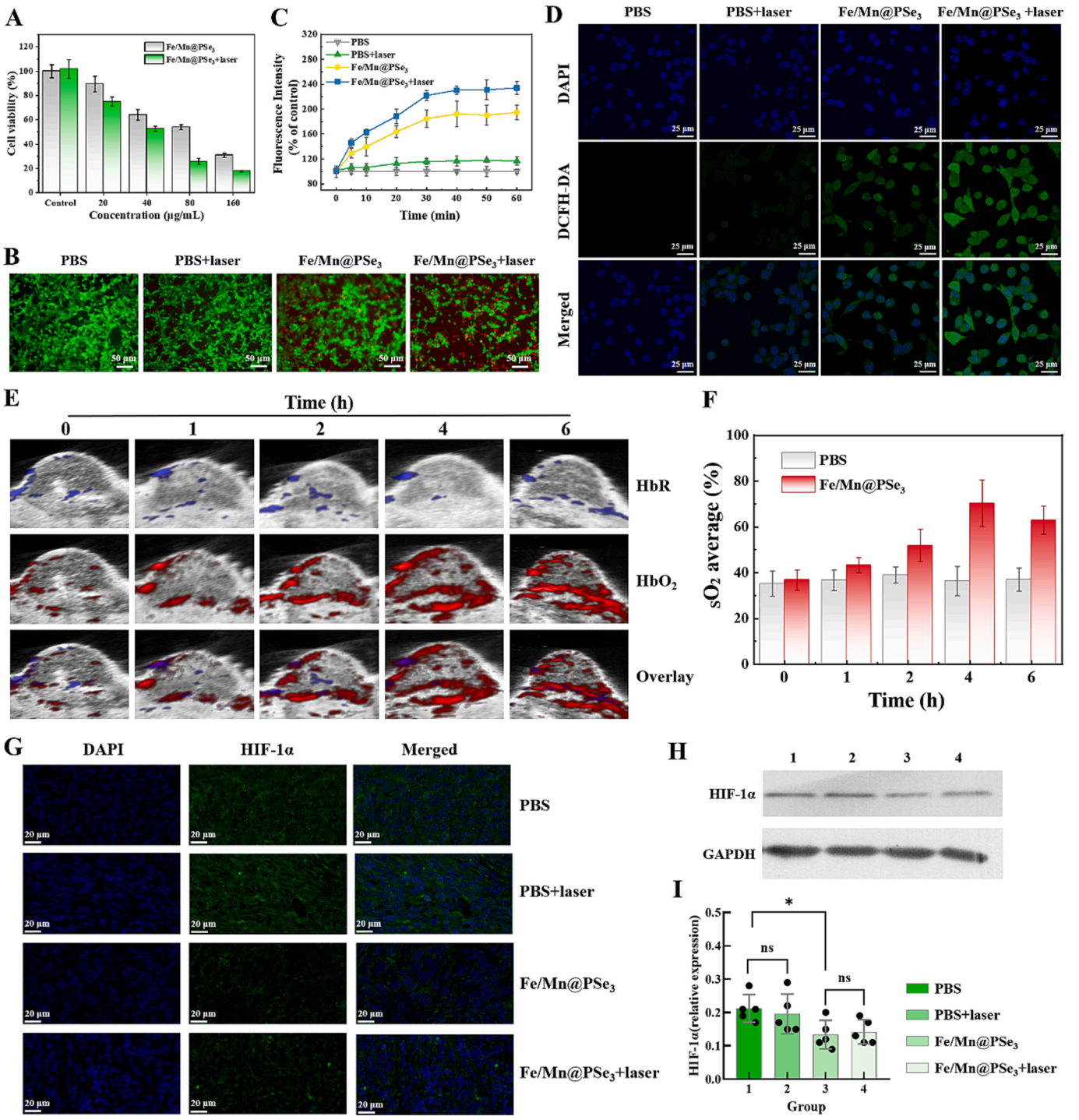

Fig. 4. ROS and O_2 generating and the consequent cell viability and hypoxia alleviation by catalytic actions of Fe/Mn@PSe_3 nanocomposites *in vitro/vivo*. (A) CT26 cell viability in simulated TME. (B) Fluorescent images of CT26 cells co-stained with calcein AM (green) and PI (red) after treatments with Fe/Mn@PSe_3. (C, D) Cytotoxic ROS level upon Fe/Mn@PSe_3 treatment as reflected in (C) plots of fluorescence intensity and (D) fluorescence images of DCFH-DA. (E) PA images of HbR and HbO_2 and (F) calculated blood oxygen saturation for monitoring oxygenation of tumor sites for 6 h after i.t. injection of Fe/Mn@PSe_3. (G-I) HIF-1α expression in tumor tissues upon Fe/Mn@PSe_3 treatment as measured by (G) immunofluorescence staining and (H) Western blotting. (I) Quantitative analysis of HIF-1α expression from Western blot result.

We then investigated the underlying mechanism of cell death induced by Fe/Mn@PSe_3 by studying the cytotoxic ROS level. As shown in Fig. 4C, a greater ROS level was observed in the group treated with Fe/Mn@PSe_3 + laser. Moreover, the ·OH-sensitive dye 2′,7′-dichlorofluorescei diacetate (DCFH-DA) was employed to detect intracellular ROS (Fig. 4D). The green fluorescence was clearly observed in cells treated by Fe/Mn@PSe_3, but not in groups treated with PBS or PBS + laser, which verified the intracellular generation of ROS by Fe/Mn@PSe_3 and explained the origin of its cytotoxicity. Elevated fluorescence intensity was observed in group treated with Fe/Mn@PSe_3 + laser, manifesting photothermal performance positively impacted ROS generation and therefore strengthen the efficacy of CDT.

2.7. In vivo hypoxia alleviation

After confirming the intracellular generation of ROS by Fe/Mn@PSe_3 and its cytotoxic effects, we then moved to evaluate the production of O_2 and its effect on hypoxia alleviation. Photoacoustic (PA) imaging was therefore performed on tumor-bearing mouse models. Oxy-hemoglobin (HbO_2) and deoxy-hemoglobin (HbR) are the two major endogenous absorbers which provide strong PA signal, and thus can be utilized to determine blood oxygen saturation (sO_2) [30,31]. The PA oxygenation map was recorded at 0, 1, 2, 4, and 6 h after i.t. injection of Fe/Mn@PSe_3. As displayed in Fig. 4E-F and S12, the injected nanocomposites produced a clear increase in HbO_2 level which reached maximum at 4 h post injection. Similarly, maximal sO_2 was seen at 4 h (~70%) and remained approximately unchanged at 6 h post injection. These results confirmed the ability of Fe/Mn@PSe_3 to reoxygenate the tumor tissue *in vivo*, indicating its' potential role in hypoxia alleviation and TME regulation.

Subsequently, hypoxia alleviation by Fe/Mn@PSe_3 was studied *via* immunofluorescence staining and Western blot analysis. It is well-established that hypoxia induces HIF-1α expression. According to Fig. 4G, the highly expressed HIF-1α, as reflected by the strong green fluorescence, was observed in tumor tissues treated by PBS or PBS +

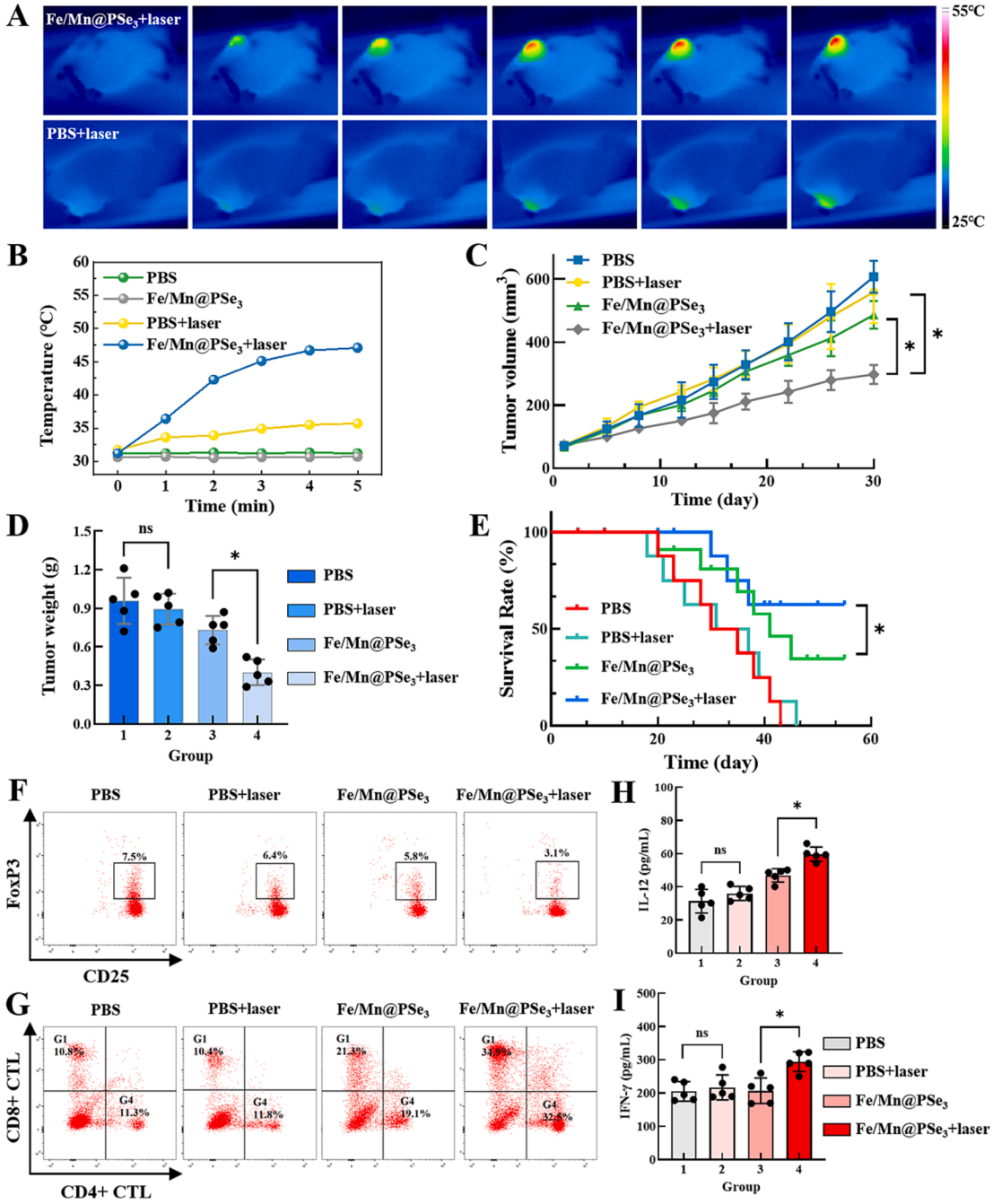

Fig. 5. *In vivo* therapeutic efficacy and the immune responses induced by Fe/Mn@PSe_3 nanocomposites. (A) Thermal imaging and (B) the corresponding temperature plots of tumor sites after i.t. injection of Fe/Mn@PSe_3 under laser irradiation. (C-E) Therapeutic effect on mice treated with i.t. administration of Fe/Mn@PSe_3: *in vivo* CT26 tumor growth curves in (C) tumor volume and (D) tumor weight; (E) Survival curve for CT26 tumor-bearing mice. (F, G) Flow cytometric analysis of Tregs and CTLs in peripheral blood of tumor-bearing mice upon Fe/Mn@PSe_3 treatment. Expression of cytokines (H) IL-12 and (I) IFN-γ in peripheral blood of tumor-bearing mice treated with Fe/Mn@PSe_3.

laser. However, upon treating with Fe/Mn@PSe_3 in the presence/absence of NIR laser, the HIF-1α expression was significantly down-regulated. Observations in Western blotting also suggest the down-regulation of HIF-1α upon Fe/Mn@PSe_3 treatment (Fig. 4 H-I). Taken together, Fe/Mn@PSe_3 treatment can reoxygenate the tumor tissue, and down-regulate HIF-1α expression *in vivo*.

2.8. *In vivo therapeutic effects of Fe/Mn@PSe_3 against tumor*

Following the extensive studies of *in vitro* catalytic properties and cytotoxicity of the nanocomposites, CT26 tumor-bearing mouse model was utilized for assessing the *in vivo* catalytic therapeutic effect of Fe/Mn@PSe_3. The mice were put into four groups at random: PBS, PBS + laser, Fe/Mn@PSe_3, and Fe/Mn@PSe_3 + laser. As shown in Fig. 5 C-D, Fe/Mn@PSe_3 treatment could inhibit growth profiles of tumor in mice, and such inhibitory was significantly enhanced when irradiated by the NIR laser (808 nm, 1.5 W cm^{-2}, 10 min). As indicated by H&E staining, cell necrosis is much more frequently seen in tumor tissues treated with Fe/Mn@PSe_3 in the presence/absence of laser irradiation than with PBS or PBS + laser (Fig. S13). Apparent localized heat generation was seen with maximum temperatures of 47.1 °C and 35.7 °C for Fe/Mn@PSe_3 + laser group and PBS + laser group, respectively (Fig. 5A-B). The obvious tumor inhibition observed for Fe/Mn@PSe_3 + laser group compared to a negligible inhibitory effect for PBS + laser group, elucidated the photothermal-augmented synergistic therapeutic efficacy. Previous studies have shown that mild hyperthermia alone (less than 50 °C) could not achieve ideal tumor ablation. However, it is a well-known adjuvant for enhancing CDT, immunotherapy, gene therapy and chemotherapy [32,33]. Based on the *in vitro* and *in vivo* experiments, the results demonstrate that the anticancer activity of FeMn@PSe_3 can be remarkably enhanced under mild hyperthermia condition. In parallel, the mouse survival rate was monitored for each group. As plotted in Fig. 5E, mice in the control PBS and PBS + laser groups all died within 46 days, which was attributed to the uncontrolled tumor growth without therapeutic intervention. A clear increase in mouse survival was seen in Fe/Mn@PSe_3 group. The survival can be further prolonged with laser irradiation, where more than 60% of the mice survived more than 55 days, verifying the efficacy of the nanocomposite-enabled *in vivo* synergistic tumor therapy.

2.9. *In vivo immune responses*

Regulatory T cells (Tregs) are a subset of T cells which take an immunosuppressive role in tumor immunity [34]. Further studies showed that Tregs in tumor hypoxia areas are also regulated by HIF-1α, elevated expression of HIF-1α leads to the enrichment of Tregs which can further aggravate immune suppression [34,35]. We showed that Fe/Mn@PSe_3 effectively alleviated tumor hypoxia and reduced HIF-1α expression. Therefore, we explored if Fe/Mn@PSe_3 can reverse hypoxia-induced immunosuppression by flow cytometry. According to Fig. 5F and S14A, Fe/Mn@PSe_3 treatment led to the decrease of FoxP3 level from 7.5% to 5.8%, a further decrease to 3.1% was demonstrated when exposed to NIR laser, indicating the ability of Fe/Mn@PSe_3 to reduce Treg suppressive function in immunosuppression.

The exhaustion of T cells from tumor hypoxia areas is a key limiting factor for the achievement of effective anticancer immunotherapy [36–38]. Given the hypoxia alleviating ability of Fe/Mn@PSe_3, we assessed the *in vivo* expression of antitumor immunologic effector cells. The elevated percentage of CD4+ and CD8 + CTL as well cytokines IFN-γ and IL-12 were seen in peripheral blood of tumor-bearing mice treated with Fe/Mn@PSe_3 (Fig. 5G-I and S14B-C). Similarly, laser irradiation further enhanced percentages of CD4+ and CD8 + to 32.5% and 34.9%, respectively, and the IFN-γ and IL-12 were also improved. Taken together, these results manifested that Fe/Mn@PSe_3 nanocomposites not only reverse immunosuppression but enhance immune responses, and both functions of Fe/Mn@PSe_3 can be further boosted by its hyperthermia feature.

2.10. *In vivo biosafety evaluation*

Biosafety and biocompatibility profiles are always the perquisites for biomedical applications especially for nanomaterials. The *in vivo* biosafety of Fe/Mn@PSe_3 nanocomposites was therefore examined in tumor-bearing mice. Histological examination of major organs was performed by Hematoxylin & Eosin (H&E) staining. No obvious histopathological lesions can be observed for mice treated with Fe/Mn@PSe_3 or Fe/Mn@PSe_3 + laser when compared to control groups (Fig. S15D). Impact on functions of liver and kidney was further studied by examining amounts of alanine aminotransferase (ALT), aspartate aminotransferase (AST) (liver function), and blood urea nitrogen (BUN) (renal function). The results showed all biochemical indicators had no significant difference among the groups (Fig. S15A-C). All in all, these results demonstrated the good biosafety profile of Fe/Mn@PSe_3 during the treatment.

3. Conclusion

In summary, guided by the structure-performance relationship of Fe-Mn-based DSACs with different Fe/Mn molar ratios in catalytic H_2O_2 transformation investigated *via* DFT calculations, we constructed a novel bimetal element-based SACs over biocompatible PSe_3 nanocomposites (Fe/Mn@PSe_3) with optimized catalytic activity, selectivity and photothermal performance. In this DSAC, each metal atom coordinates with six Se atoms, forming identical Fe-Se_6 and Mn-Se_6 centers, thus serving as an ideal platform for digging into the reaction mechanisms and controlling its catalytic performance. Assisted by the acidic conditions in TME, the optimized well-defined DSACs can effectively catalyze TME H_2O_2 to generate O_2 to alleviate tumor hypoxia and thus alleviate the immunosuppressive effect. Besides, in response to the elevated H_2O_2 level in TME, the DSACs can generate ·OH to trigger CDT, and tumor-suppressing effects can be further improved by mild hyperthermia. This work provides a good paradigm for exploring the biomedical nanomaterials: starting from TME factors, focusing on structure-antitumor performance and biosafety issues, adopting materials with essential elements and controlled activity & selectivity.

4. Experimental section/methods

4.1. *Materials*

Powder of Iron, Manganese, Selenium and Phosphorus were purchased from Alfa Aesar Company. All other chemicals and solvents were purchased from Sigma-Aldrich Chemical Company. All chemicals were used without further purification. All media for cell culture were purchased from Thermo Fisher Scientific Corporation.

4.2. *Fabrication of Fe/Mn@PSe_3*

Firstly, the high purity elementary substance (Fe, Mn, P, Se) were weighed in molar ratios (0.5: 0.5: 1: 3) and loaded the above mixed substance into the quartz tube, and then volumized to less than 0.001 Pa. Secondly, the substances were heated to 700 °C with a temperature increase rate of 5 °C per minute and kept warm for 100 h to ensure sufficient reaction to obtain the required compound. The reaction was then naturally cooled to room temperature, and the quartz tube was broken to collect the powder (Fe/Mn@PSe_3).

10 mg Fe/Mn@PSe_3 powder were ground to a fine powder in a mortar. The fine power was then exfoliated *via* sonication for around 48 h using N-methyl-2-pyrrolidone (NMP) (10 mL) as a solvent. The resulting solution was sent to centrifuge at 4000 rpm for the removal of large bulk. The precipitation was collected at a higher speed (14000 rpm) centrifugation for a longer time (30 min) and then washed several

times by a mixed solution of water and ethanol. With the aim to improve the stability, 10 mg Fe/Mn@PSe_3 nanocomposites was dispersed in PVP (1 mg mL^{-1}) and stirred at room temperature for 24 h. After removal of the excess PVP by centrifugation, the PVP-modified Fe/Mn@PSe_3 nanocomposites were obtained.

4.3. Characterizations of Fe/Mn@PSe_3

Structural characterization of Fe/Mn@PSe_3 nanocomposites, such as morphology, size distribution, thickness, elemental composition, metal oxidation state, were performed using SEM (TESCAN VEGA3), STEM (Jeol JEM-2100F), GE AKTA Pure 25L Chromatography System coupled with the DAWN HELEOS 8 + Eight-Angle Laser Light Scattering Instrument, Zetasizer Particle Size Analyzer (Malvern Mastersizer 3000), AFM (Bruker Multimode 8 SPM).

4.4. EXAFS measurements

EXAFS for Fe/Mn@PSe_3 nanocomposites were performed at 21A beamline at Taiwan Photon Source. Four-bounce channel-cut Si (1 1 1) monochromator is used for mono-beam X-ray absorption spectroscopy. The end-station is equipped with three ionization chambers and Lytle/SDD type detector, for the transmission and fluorescence mode XAFS. Monochromatic photon flux on the sample ranges between 6 keV and 27 keV at about $1 \times 10^{11} \sim 3 \times 10^{9}$ photon/s.

4.5. Photothermal effects

Aqueous solution of Fe/Mn@PSe_3 nanocomposites at different concentrations (0, 62.5, 125, 250 and 500 ppm), were irradiated with 808 nm NIR laser (2.0 W cm^{-2}) for 5 min. The 5-min irradiation was also performed for Fe/Mn@PSe_3 with the increase of power densities including 0.5, 1.0, 1.5 and 2.0 W cm^{-2}. In addition, heating–cooling cycle of Fe/Mn@PSe_3 were repeated for three times under 808 nm laser irradiation, for the evaluation of photothermal conversion stability of Fe/Mn@PSe_3. Temperature changes and the corresponding picture were obtained using a Fluke Ti450 Thermal Imager, for calculating the photothermal conversion efficiency (η) of Fe/Mn@PSe_3 according to the equation shown below [24]:

$$\eta = \frac{\boldsymbol{hA}(\boldsymbol{T_{max}} - \boldsymbol{T_{amb}}) - \boldsymbol{Q_0}}{\boldsymbol{I}(1 - 10^{-A_\lambda})} \quad (1)$$

where h is the coefficient of heat transfer, A is the surface area of the container, T_{max} and T_{amb} represent the maximum temperature of Fe/Mn@PSe_3 and the ambient temperature respectively, Q_0 is the heat associated with the light absorbance of the solvent, I is the power density of NIR laser, and A_λ is the absorbance of Fe/Mn@PSe_3 at the wavelength 808 nm.

4.6. Detection of the oxygen generation

To detect the oxygen generation, Fe@PSe_3, Mn@PSe_3, and Fe/Mn@PSe_3 (1 mg) were incubated at acidic buffered solution (pH 6.5), to which was added 100 μM H_2O_2 solution. The real-time dissolved O_2 at both conditions were measured directly at different time points (0, 1, 2, 4, 6, 8, and 10 min) using a JPBJ-608 portable Dissolved Oxygen Meter (Yantai Stark Instrument, China).

4.7. Detection of the hydroxyl radical generation

TMB assay was used to detect the production of ROS by colorimetric reaction, which can be oxidized by ROS to oxTMB with absorption maximum at 652 nm. The absorbance spectrum of Fe@PSe_3, Mn@PSe_3, Fe/Mn@PSe_3, and Fe/Mn@PSe_3 + laser was measured using a UV–vis spectrophotometer [27–29]. ESR was used to verify the production of ·OH. To a TME simulating solution (pH6.5, 100 μM H_2O_2) containing 100 μM DMPO, where DMPO was used as the ·OH trapping agent, was added 100 μg mL^{-1} Fe@PSe_3, Mn@PSe_3 and Fe/Mn@PSe_3 respectively. The mixed solutions were swiftly and uniformly shaken before being transferred to a quartz tube for ESR test [27–29].

4.8. POD-like activity and enzymatic kinetic experiments

POD-like activity assays of Fe/Mn@PSe_3 were carried out with H_2O_2 as the reaction substrate and TMB as chromogenic agent [27–29]. In brief, Fe/Mn@PSe_3, TMB (1 mM) and various H_2O_2 concentrations (0.1 mM, 0.2 mM, 0.4 mM, 0.6 mM, 0.8 mM, and 1.0 mM) were added to 2 mL of acidic PBS solution at room temperature. The absorbance at 652 nm was recorded *via* UV–vis spectrophotometer. By fitting absorbance data to the Michaelis-Menten equation, the steady-state kinetic parameters of Fe/Mn@PSe_3 were determined. The Beer-Lambert Law was used to compute the initial reaction rates (V_0) of varied H_2O_2 concentrations based on changes in absorbance. The mathematical equation that describes the relationship between reaction rates and H_2O_2 concentrations was fitted to obtain the Michaelis-Menten kinetic curve. The K_m and V_{max} were determined using the Lineweaver-Burk plot.

$$A = \varepsilon bc \quad (2)$$

$$v_0 = \frac{v_{max} \bullet [S]}{k_m + [S]} \quad (3)$$

$$\frac{1}{v_0} = \frac{k_m}{v_{max}} \bullet \frac{1}{[S]} + \frac{1}{v_{max}} \quad (4)$$

In these equations, ε is the molar absorption coefficient of oxTMB (39,000 M^{-1} cm^{-1}), [S] is the substrate concentrations.

4.9. Computational method

The Vienna Ab Initio Package [39,40] was used for all DFT calculations within the generalized gradient approximation using the Perdew-Burke-Ernzerhof [41] formulation. The projected augmented wave potentials [42,43] was used to describe the ionic cores. The valence electrons were taken into account using a plane wave basis set with a kinetic energy cutoff of 400 eV. Partial occupancies of the Kohn-Sham orbitals were allowed using the Gaussian smearing method and a width of 0.05 eV. The electronic energy was considered self-consistent in cases of energy change less than 10^{-5} eV. And, a geometry optimization was considered convergent in cases of force change less than 0.02 eV/Å. Grimme's DFT-D3 methodology [44] was employed to describe the dispersion interactions.

The equilibrium lattice constants of hexagonal $MPSe_3$ unit cell were optimized, when using a 3 × 3 × 1 Monkhorst-Pack k-point grid for Brillouin zone sampling, to be a = b = 6.172 Å, c = 17.663 Å. We then used it to construct a $FePSe_3$(0 0 1) surface model with $p(2 \times 2)$ periodicity in the × and y directions and 1 stoichiometric layer in the z direction separated by a vacuum layer in the depth of 15 Å to separate the surface slab from its periodic duplicates. In model 1, one Se atom was removed in order to form a Se vacancy. Half of the Fe atoms in model 1 were replaced by Mn atoms to genarate model 2. During structural optimizations, a 2 × 2 × 1 k-point grid in the Brillouin zone was used for k-point sampling, and all atoms were allowed to relax.

4.10. In vitro anticancer efficacy

The CT26 cancer cells were obtained from FuHeng Biology Co., Ltd. (Shanghai, China). CT26 cancer cells were cultured as previously reported [24]. Different concentrations of Fe/Mn@PSe_3 nanocomposites including 0, 20, 40, 80, and 160 μg mL^{-1}, were used to treat CT26 cells seeded in 96-well plates (5000 cells $well^{-1}$). After 8 h, the incubated cells were exposed to 808 nm NIR laser (1.5 W cm^{-2}) for 10 min. Later,

the cells were sent to the incubator for another 16 h. MTT assay was applied to determine the cytotoxicity of Fe/Mn@PSe_3 towards cancer cells. In addition, 2 fluorescent probes calcein AM and PI, were employed for the visual measurement of cell viability as previously reported [45], for which the fluorescence images were measured using fluorescence microscopy (ZEISS AXIO Observer.Z1). All experiments were repeated three times.

4.11. In vitro determination of reactive oxygen species

To determine the generated ROS *in vitro*, CT26 cells treated with different groups (PBS, PBS + laser, Fe/Mn@PSe_3, Fe/Mn@PSe_3 + laser) were stained with DCFH-DA (10 μM) (Fe/Mn@PSe_3 concentration: 160 μg mL^{-1}; laser dosage: 808 nm, 1.5 W cm^{-2}, 10 min). After 30 min incubation, DCF-induced green fluorescence was captured by Leica TCS SPE confocal microscope. Emission intensity of DCF at 525 nm was tested using Varioskan LUX Multimode Microplate Reader (Thermo Scientific, λ_{ex}: 488 nm).

4.12. In vivo anticancer efficacy

To establish the CT26 tumor-bearing mice, 1×10^6 CT26 cells suspended in 100 μL of serum-free RPMI medium were subcutaneously implanted into the right hind limb of 5 to 6 week-old male C57BL/6J mice. After 7 days, when tumors had grown to an average volume of ~ 60 mm^3, mice were randomly distributed into four groups ($n = 5$ per group) and intratumorally injected with 100 μL PBS, PBS + laser, Fe/Mn@PSe_3, Fe/Mn@PSe_3 + laser (1 mg kg^{-1}) two times per week for the duration of 30 days. At 30 min post injection, tumor tissues from two groups (PBS + laser, Fe/Mn@PSe_3 + laser) were received with a NIR irradiation (808 nm, 1.5 W cm^{-2}, 10 min). During the course of treatment, body weight and tumor volume of mice were weighted and recorded, where the tumor volume were calculated as (length × $width^2$)/2. Mice were sacrificed after the 30-day treatment. Main organs, blood, and tumor tissues were collected for further analysis. The investigator was blind to the grouping during the experiment and analysis of data. A daily record on mice mortality was conducted. After 55-days treatment, Kaplan-Meier estimate was employed to analyze mice survival. All the animal experiments were performed under the approvement of The Hong Kong Polytechnic University Animal Study Committee.

4.13. Down-regulation of HIF-1α expression by Fe/Mn@PSe_3

The collected tumor tissues were fixed with 4% paraformaldehyde (PFA) solution for the preparation of paraffin slices. Afterwards, immunofluorescence method was applied to examine expression of HIF-1α as an effect of Fe/Mn@PSe_3. In addition, total proteins were extracted from fresh tumor tissue, and then western blotting was employed to measure HIF-1α level. HIF-1α XP® Rabbit mAb antibody from Cell Signaling Technology was used for immunofluorescence.

4.14. Immune response induced by Fe/Mn@PSe_3

After the 30-day treatment, peripheral blood was harvested from mice *via* standard eye bleed protocol, for which the mononuclear cells were removed by a density gradient centrifugation using Ficoll-Hypaque solution. Flow cytometric study was used to measure the CD4+ and CD8 + CTLs presented in peripheral blood (CD4-FITC Monoclonal Antibody, CD8a-APC Monoclonal Antibody, Thermo Fisher Scientific Corporation). Similarly, Treg cells (CD4+ CD25 + FoxP3 + cell) in the blood sample were also evaluated (CD4-FITC Monoclonal Antibody, CD25-APC Monoclonal Antibody, FoxP3 Monoclonal Antibody, PE-Cyanine5.5, Thermo Fisher Scientific Corporation). In addition, to measure levels of cytokines including IL-12 and IFN-γ in serum, the peripheral blood was centrifuged, and ELISA-based assay was applied.

4.15. Biosafety of Fe/Mn@PSe_3

Two normal cell lines, human umbilical vein endothelial cells (HUVECs) and embryonic fibroblast cells (NIH 3 T3), were used to evaluate the biosafety of Fe/Mn@PSe_3 to normal cells through MTT experiments. Moreover, the collected main organs such as heart, liver, spleen, lung, and kidney collected above were fixed with 4% PFA solution for the preparation of paraffin slices. H&E staining was performed for histological examination of the main organs upon Fe/Mn@PSe_3 treatment. The collected whole blood was used for analysis of levels of AST, ALT, and BUN by Automatic Biochemical Analyzer (Hitachi 7600).

4.16. Statistical analysis

All statistical analysis were performed using softares including GraphPad Prism 8, Origin 9, and SPSS22.0. Data are expressed as mean ± SD, a one-way ANOVA was employed to test for differences among groups, and the Fisher's LSD method was employed for comparison of means from multiple processes, *P* less than 0.05 was considered statistically significant. Kaplan-Meier estimate was employed for the analysis of mice survival.

CRediT authorship contribution statement

Xueyang Fang: Conceptualization, Data curation, Funding acquisition, Investigation, Writing – original draft. **Decai Yang:** Data curation, Funding acquisition, Writing – original draft. **Xianlin Wu:** Formal analysis, Methodology, Writing – original draft. **Kwok-Ho Lui:** Writing – review & editing. **Xin Li:** Investigation. **Wai-Sum Lo:** Investigation. **Chenxi Li:** Investigation. **Yuanyuan Zhang:** Methodology. **Guohui Nie:** Resources, Supervision. **Lijun Jiang:** Methodology, Funding acquisition, Writing – original draft. **Yanjuan Gu:** Resources, Supervision, Writing – original draft. **Bin Zhang:** Conceptualization, Funding acquisition, Resources, Supervision, Writing – original draft. **Wing-Tak Wong:** Resources, Supervision.

Declaration of Competing Interest

The authors declare that they have no known competing financial interests or personal relationships that could have appeared to influence the work reported in this paper.

Data availability

Data will be made available on request.

Acknowledgements

We acknowledge the grants from the National Key Research and Development Program of China (2022YFA0912500), Shenzhen Science and Technology Program (RCBS20221008093329063), National Natural Science Foundation of China (32071376, 32301128, 82192865, 52203335 and 32200074), Postdoctoral Science Foundation of China (2022M722206, 2022M722208), Basic and Applied Basic Research Foundation of Guangdong Province (2022A1515110803, 2020A 1515110749), Hubei Key Laboratory of Genetic Regulation and Integrative Biology (GRIB202219), Shenzhen Science and Technology Innovation Committee (ZDSYS201707281114196, KCXFZ20201221173413038 and JCYJ20190806163805286), and Science and Technology Projects in Guangzhou (202102010103). This work is also supported by Shenzhen High-level Hospital Construction Fund, Development and Reform Commission of Shenzhen Municipality.

Appendix A. Supplementary data

Supplementary data to this article can be found online at https://doi.org/10.1016/j.cej.2023.145675.

References

[1] L. Bejarano, M.J.C. Jordao, J.A. Joyce, Therapeutic Targeting of the Tumor Microenvironment, Cancer Discov. 11 (2021) 933–959, https://doi.org/10.1158/2159-8290.CD-20-1808.

[2] S. Grisaru-Tal, M.E. Rothenberg, A. Munitz, Eosinophil-lymphocyte interactions in the tumor microenvironment and cancer immunotherapy, Nat. Immunol. 23 (2022) 1309–1316, https://doi.org/10.1038/s41590-022-01291-2.

[3] A. Emami Nejad, S. Najafgholian, A. Rostami, A. Sistani, S. Shojaeifar, M. Esparvarinha, R. Nedaeinia, S. Haghjooy Javanmard, M. Taherian, M. Ahmadlou, R. Salehi, B. Sadeghi, M. Manian, The role of hypoxia in the tumor microenvironment and development of cancer stem cell: A novel approach to developing treatment, Cancer Cell Int. 21 (2021) 62, https://doi.org/10.1186/s12935-020-01719-5.

[4] P. Zheng, M. Fan, H. Liu, Y. Zhang, X. Dai, H. Li, X. Zhou, S. Hu, X. Yang, Y. Jin, N. Yu, S. Guo, J. Zhang, X.J. Liang, K. Cheng, Z. Li, Self-Propelled and Near-Infrared-Phototaxic Photosynthetic Bacteria as Photothermal Agents for Hypoxia-Targeted Cancer Therapy, ACS Nano 15 (2021) 1100–1110, https://doi.org/10.1021/acsnano.0c08068.

[5] W. Zeng, P. Liu, W. Pan, S.R. Singh, Y. Wei, Hypoxia and hypoxia inducible factors in tumor metabolism, Cancer Lett. 356 (2015) 263–267, https://doi.org/10.1016/j.canlet.2014.01.032.

[6] A. Palazon, A.W. Goldrath, V. Nizet, R.S. Johnson, HIF transcription factors, inflammation, and immunity, Immunity 41 (2014) 518–528, https://doi.org/10.1016/j.immuni.2014.09.008.

[7] A. Mancino, T. Schioppa, P. Larghi, F. Pasqualini, M. Nebuloni, I.H. Chen, S. Sozzani, J.M. Austyn, A. Mantovani, A. Sica, Divergent effects of hypoxia on dendritic cell functions, Blood 112 (2008) 3723–3734, https://doi.org/10.1182/blood-2008-02-142091.

[8] S.-L. Li, P. Jiang, F.-L. Jiang, Y. Liu, Recent Advances in Nanomaterial-Based Nanoplatforms for Chemodynamic Cancer Therapy, Adv. Funct. Mater. 31 (2021) 2100243, https://doi.org/10.1002/adfm.202100243.

[9] L.-H. Fu, Y. Wan, C. Qi, J. He, C. Li, C. Yang, H. Xu, J. Lin, P. Huang, Nanocatalytic Theranostics with Glutathione Depletion and Enhanced Reactive Oxygen Species Generation for Efficient Cancer Therapy, Adv. Mater. 33 (7) (2021) 2006892.

[10] Y. Ai, Z.-N. Hu, X. Liang, H.-B. Sun, H. Xin, Q. Liang, Recent Advances in Nanozymes: From Matters to Bioapplications, Adv. Funct. Mater. 32 (14) (2022).

[11] J. Ye, W. Lv, C. Li, S. Liu, X. Yang, J. Zhang, C. Wang, J. Xu, G. Jin, B. Li, Y. Fu, X. Liang, Tumor Response and NIR-II Photonic Thermal Co-Enhanced Catalytic Therapy Based on Single-Atom Manganese Nanozyme, Adv. Funct. Mater. 32 (2022) 2206157, https://doi.org/10.1002/adfm.202206157.

[12] L. Li, L. Cao, X. Xiang, X. Wu, L. Ma, F. Chen, S. Cao, C. Cheng, D. Deng, L. Qiu, ROS-Catalytic Transition-Metal-Based Enzymatic Nanoagents for Tumor and Bacterial Eradication, Adv. Funct. Mater. 32 (2022) 2107530, https://doi.org/10.1002/adfm.202107530.

[13] J. Li, M.F. Stephanopoulos, Y. Xia, Introduction: Heterogeneous Single-Atom Catalysis, Chem. Rev. 120 (2020) 11699–11702, https://doi.org/10.1021/acs.chemrev.0c01097.

[14] S. Ding, Y. Guo, M.J. Hülsey, B. Zhang, H. Asakura, L. Liu, Y. Han, M. Gao, J.-Y. Hasegawa, B. Qiao, T. Zhang, N. Yan, Electrostatic Stabilization of Single-Atom Catalysts by Ionic Liquids, Chem-Us 5 (2019) 3207–3219, https://doi.org/10.1016/j.chempr.2019.10.007.

[15] H. Xiang, W. Feng, Y.u. Chen, Single-Atom Catalysts in Catalytic Biomedicine, Adv. Mater. 32 (8) (2020) 1905994.

[16] J. Pei, R. Zhao, X. Mu, J. Wang, C. Liu, X.D. Zhang, Single-atom nanozymes for biological applications, Biomater. Sci. 8 (2020) 6428–6441, https://doi.org/10.1039/d0bm01447h.

[17] M. Huo, L. Wang, Y. Wang, Y. Chen, J. Shi, Nanocatalytic Tumor Therapy by Single-Atom Catalysts, ACS Nano 13 (2019) 2643–2653, https://doi.org/10.1021/acsnano.9b00457.

[18] Y. Zhu, W. Wang, J. Cheng, Y. Qu, Y. Dai, M. Liu, J. Yu, C. Wang, H. Wang, S. Wang, C. Zhao, Y. Wu, Y. Liu, Stimuli-Responsive Manganese Single-Atom Nanozyme for Tumor Therapy via Integrated Cascade Reactions, Angew. Chem. Int. Ed. Engl. 60 (2021) 9480–9488, https://doi.org/10.1002/anie.202017152.

[19] W. Zhang, Y. Chao, W. Zhang, J. Zhou, F. Lv, K. Wang, F. Lin, H. Luo, J. Li, M. Tong, E. Wang, S. Guo, Emerging Dual-Atomic-Site Catalysts for Efficient Energy Catalysis, Adv. Mater. 33 (2021) e2102576.

[20] J. Fu, J. Dong, R. Si, K. Sun, J. Zhang, M. Li, N. Yu, B. Zhang, M.G. Humphrey, Q. Fu, J. Huang, Synergistic Effects for Enhanced Catalysis in a Dual Single-Atom Catalyst, ACS Catal. 11 (2021) 1952–1961, https://doi.org/10.1021/acscatal.0c05599.

[21] E.A. Moges, C.-Y. Chang, W.-H. Huang, K. Lakshmanan, Y.A. Awoke, C.-W. Pao, M.-C. Tsai, W.-N. Su, B.J. Hwang, Sustainable Synthesis of Dual Single-Atom Catalyst of Pd-N_4/Cu-N_4 for Partial Oxidation of Ethylene Glycol, Adv. Funct. Mater. 32 (2022) 2206887, https://doi.org/10.1002/adfm.202206887.

[22] M. Zhao, R. Yang, Y. Wei, J. Su, X. Wang, N. Zhang, P. Sun, D. Chen, Y. Zhao, Dual isolated bimetal single-atom catalysts for tumor ROS cycle and parallel catalytic therapy, Nano Today 44 (2022), 101493, https://doi.org/10.1016/j.nantod.2022.101493.

[23] C. Yang, Y. Luo, H. Shen, M. Ge, J. Tang, Q. Wang, H. Lin, J. Shi, X. Zhang, Inorganic nanosheets facilitate humoral immunity against medical implant infections by modulating immune co-stimulatory pathways, Nat. Commun. 13 (2022) 4866, https://doi.org/10.1038/s41467-022-32405-x.

[24] X.Y. Fang, X.L. Wu, Z.D. Li, L.J. Jiang, W.S. Lo, G.M. Chen, Y.J. Gu, W.T. Wong, Biomimetic Anti-PD-1 Peptide-Loaded 2D $FePSe_3$ Nanosheets for Efficient Photothermal and Enhanced Immune Therapy with Multimodal MR/PA/Thermal Imaging, Adv. Sci. 8 (2021) 2003041, https://doi.org/10.1002/advs.202003041.

[25] J. Guo, S. Jin, G. Wang, S. Wang, K. Zhu, T. Zhou, M. He, X. Chen, Superconductivity in the iron selenide $K_xFe_2Se_2$ ($0 \leq x \leq 1.0$), Phys. Rev. B 82 (2010) 180520(R), https://doi.org/10.1103/PhysRevB.82.180520.

[26] W. Sinkler, S.I. Sanchez, S.A. Bradley, J. Wen, B. Mishra, S.D. Kelly, S.R. Bare, Aberration-Corrected Transmission Electron Microscopy and In Situ XAFS Structural Characterization of Pt/γ-Al_2O_3 Nanoparticles, ChemCatChem 7 (2015) 3779–3787, https://doi.org/10.1002/cctc.201500784.

[27] Y. Liu, B. Wang, J. Zhu, X. Xu, B. Zhou, Y. Yang, Single-Atom Nanozyme with Asymmetric Electron Distribution for Tumor Catalytic Therapy by Disrupting Tumor Redox and Energy Metabolism Homeostasis, Adv. Mater. 35 (2023) e2208512.

[28] R. Niu, Y. Liu, Y. Wang, H. Zhang, An Fe-based single-atom nanozyme with multi-enzyme activity for parallel catalytic therapy via a cascade reaction, Chem. Commun. 58 (2022) 7924–7927, https://doi.org/10.1039/d2cc02975h.

[29] Y. Liu, R. Niu, R. Deng, S. Song, Y. Wang, H. Zhang, Multi-enzyme Co-expressed Dual-Atom Nanozymes Induce Cascade Immunogenic Ferroptosis via Activating Interferon-gamma and Targeting Arachidonic Acid Metabolism, J. Am. Chem. Soc. 145 (2023) 8965–8978, https://doi.org/10.1021/jacs.2c13689.

[30] S. Mallidi, G.P. Luke, S. Emelianov, Photoacoustic imaging in cancer detection, diagnosis, and treatment guidance, Trends Biotechnol. 29 (2011) 213–221, https://doi.org/10.1016/j.tibtech.2011.01.006.

[31] F. Cao, Z. Qiu, H. Li, P. Lai, Photoacoustic Imaging in Oxygen Detection, Appl. Sci. 7 (2017) 1262, https://doi.org/10.3390/app7121262.

[32] X. Zhang, J. Du, Z. Guo, J. Yu, Q. Gao, W. Yin, S. Zhu, Z. Gu, Y. Zhao, Efficient Near Infrared Light Triggered Nitric Oxide Release Nanocomposites for Sensitizing Mild Photothermal Therapy, Adv. Sci. 6 (2019) 1801122, https://doi.org/10.1002/advs.201801122.

[33] G. Gao, X. Sun, G. Liang, Nanoagent-Promoted Mild-Temperature Photothermal Therapy for Cancer Treatment, Adv. Funct. Mater. 31 (2021) 2100738, https://doi.org/10.1002/adfm.202100738.

[34] Y. Takeuchi, H. Nishikawa, Roles of regulatory T cells in cancer immunity, Int. Immunol. 28 (2016) 401–409, https://doi.org/10.1093/intimm/dxw025.

[35] R.C. Augustin, G.M. Delgoffe, Y.G. Najjar, Characteristics of the Tumor Microenvironment That Influence Immune Cell Functions: Hypoxia, Oxidative Stress, Metabolic Alterations, Cancers 12 (2020) 3802, https://doi.org/10.3390/cancers12123802.

[36] S. Peng, F. Xiao, M. Chen, H. Gao, Tumor-Microenvironment-Responsive Nanomedicine for Enhanced Cancer Immunotherapy, Adv. Sci. 9 (2022) 2103836, https://doi.org/10.1002/advs.202103836.

[37] C.C. Caldwell, H. Kojima, D. Lukashev, J. Armstrong, M. Farber, S.G. Apasov, M. V. Sitkovsky, Differential Effects of Physiologically Relevant Hypoxic Conditions on T Lymphocyte Development and Effector Functions, J. Immunol. 167 (2001) 6140, https://doi.org/10.4049/jimmunol.167.11.6140.

[38] N. Imai, I. Tawara, M. Yamane, D. Muraoka, H. Shiku, H. Ikeda, CD4+ T cells support polyfunctionality of cytotoxic CD8+ T cells with memory potential in immunological control of tumor, Cancer Sci. 111 (2020) 1958–1968, https://doi.org/10.1111/cas.14420.

[39] G. Kresse, J. Furthmüller, Efficiency of ab-initio total energy calculations for metals and semiconductors using a plane-wave basis set, Comp. Mater. Sci. 6 (1) (1996) 15–50.

[40] G. Kresse, J. Furthmüller, Efficient iterative schemes for ab initio total-energy calculations using a plane-wave basis set, Phys. Rev. B 54 (1996) 11169–11186, https://doi.org/10.1103/PhysRevB.54.11169.

[41] J.P. Perdew, K. Burke, M. Ernzerhof, Generalized Gradient Approximation Made Simple, Phys. Rev. Lett. 77 (1996) 3865–3868, https://doi.org/10.1103/PhysRevLett.77.3865.

[42] G. Kresse, D. Joubert, From ultrasoft pseudopotentials to the projector augmented-wave method, Phys. Rev. B 59 (1999) 1758–1775, https://doi.org/10.1103/PhysRevB.59.1758.

[43] P.E. Blochl, Projector augmented-wave method, Phys. Rev. B 50 (1994) 17953–17979, https://doi.org/10.1103/physrevb.50.17953.

[44] S. Grimme, J. Antony, S. Ehrlich, H. Krieg, A consistent and accurate ab initio parametrization of density functional dispersion correction (DFT-D) for the 94 elements H-Pu, J. Chem. Phys. 132 (2010), https://doi.org/10.1063/1.3382344.

[45] X.Y. Fang, K.H. Lui, S.Y. Li, W.S. Lo, X. Li, Y.J. Gu, W.T. Wong, Multifunctional Nanotheranostic Gold Nanocage/Selenium Core-Shell for PAI-Guided Chemo-Photothermal Synergistic Therapy in vivo, Int. J. Nanomed. 15 (2020) 10271–10284, https://doi.org/10.2147/Ijn.S275846.